THE POTENTIAL FOR BLOOD-BRAIN-BARRIER (BBB) DISRUPTION DURING 3D TRANSCRANIAL ULTRASOUND SUPER-RESOLUTION IMAGING

Hanjoo R. Lee

A thesis submitted to the faculty at the University of North Carolina at Chapel Hill in partial fulfillment of the requirements for the degree of Master of Science in the Joint Biomedical Engineering Department in the University of North Carolina at Chapel Hill.

Chapel Hill
2023

Approved by

Paul A. Dayton

Gianmarco F. Pinton

Virginie Papadopoulou

Kennita Johnson

ABSTRACT

Hanjoo R. Lee: The Potential for Blood-Brain-Barrier (BBB) Disruption During 3D Transcranial Ultrasound Super-Resolution Imaging
(Under the direction of Paul A. Dayton and Gianmarco F. Pinton)

Super-Resolution (SR) ultrasound dramatically improves the resolution of microvascular images beyond the diffraction limit. It is well-established that ultrasound with contrast agents, like those used in SR, can open the blood brain barrier (BBB) under certain conditions. This study aims to quantify potential BBB disruption during 3D transcranial ultrasound SR as a function of mechanical index (MI) and pressure distribution. Mice were imaged using conventional 3D SR sequences. BBB disruption was quantified through fluorescence imaging of dye extravasation for 0-0.78 transmit MI (measured in water). Results suggest 3D SR at 0.78 MI induced BBB opening; however, imaging was achievable without significant dye extravasation below 0.78. Hydrophone measurements and 3D modeling were performed to estimate local pressure distributions in the brain. Estimates of local MI within the brain indicate 0.44-0.53 MI generates BBB bioeffects. Results may help inform parameter choices for effectively conducting transcranial 3D SR imaging to avoid BBB opening.

To my mother, who inspired me to help others through research by seeing her own passion and work and her encouragement to be curious and learn. To my friends, who I am so grateful for, showing me the joys of humanity and what I want to protect through research.

TABLE OF CONTENTS

LIST OF TABLES…….....vii

LIST OF ABBREVIATIONS……..ix

CHAPTER 1: INTRODUCTION & BACKGROUND……1

1.1 Medical Ultrasound.....1

1.2 Super Resolution.....1

1.3 Blood-Brain-Barrier.....2

1.4 Blood-Brain-Barrier Disruption.....3

1.5 Thesis Outline.....4

CHAPTER 2: METHODOLOGY……7

2.1 Animal Experiments..... 7

2.2 Ultrasound Imaging..... 9

2.3 Evaluation of BBB disruption..... 10

2.4 Super Resolution Processing..... 11

2.5 Ex-Vivo Characterization..... 11

2.6 3D Simulations..... 13

CHAPTER 3: RESULTS & DISCUSSION……..15

3.1 BBB Disruption Analysis 15

3.2 Super Resolution..... 19

3.3 Hydrophone Characterization 19

3.4 3D Simulations..... 20

3.5 BBB Disruption Discussion..... 21

3.6 Super Resolution Discussion 23

3.7 Ultrasound Transmission Through the Murine Skull 24

CHAPTER 4: CONCLUSION…..……..…27

REFERENCES 29

LIST OF FIGURES

Figure 1: (a) Schematic of ultrasound (US) imaging and infusion setup. CD-1 mice were injected with 2 % Evans blue dye then followed by a bolus injection of decafluorobutane microbubbles (MB). The MBs were then placed onto the infusion pump (15uL/min) for the rest of the time the animal was placed for acquisition. Volumetric ultrasound images were acquired using plane wave compounding using single cycle pulses (5 angles, 2500 Hz pulse repetition frequency, 500 volumes per second). (b) Schematic of the in-vivo workflow where the mouse brains were fixed in PBF and then fluorescence images were taken, sectioned, then imaged again. (c) Hydrophone characterization timeline starting from in-vivo experiment to skull extraction and cleaning to CT scans taken and then hydrophone characterization. Specimen were stored in 100% phosphate buffered saline until time of scanning and time for characterization. 7

Figure 2: Whole brain fluorescence images showing the fluorescence intensity distribution per group. As mechanical index (MI) increases, so does the fluorescence intensity of the whole brain view of the mouse brain indicating increasing dye extravasation. 15

Figure 3: (a) Fluorescence images of all 8 coronal brain sections of one representative brain from each experimental group. (b) Heatmap of the fluorescence intensity from every section averaged from all 8 mouse brains per group. MI: mechanical index. 16

Figure 4: SECTIONED FLUORESCENCE IMAGES from the first rounds of the in-vivo study where each column represents 1 group (Evans blue dye and no microbubbles, Evans blue dye with microbubbles, 0.28 MI, 0.64 MI, and 0.78 MI). Dye extravasation increases with MI like in Fig 5a. The Evans blue dye with microbubbles group was found to have identical dye extravasation with the Evans blue dye with no microbubbles so the study was continued with the Evans blue dye with no microbubbles as the control group. The region of interest (ROI) rectangles can also be seen demonstrating how the ROI was drawn. 16

Figure 5: (a) Whole brain fluorescence intensity per experimental group. A significant increase in fluorescence intensity was observed for both 0.64 and 0.78 MI (MI = Mechanical Index) compared to the control group. (b) fluorescence intensity for a single brain section 2 mm in front of bregma, showing a significant increase in fluorescence intensity for 0.78 MI vs the control group. 17

Figure 6: Graphs of each section and results of Dunnet multiple comparisons test, shown as * for significant dye extravasation ($p<0.05$) from control. Every section except for section 1 showed significant dye extravasation for 0.78 MI and 2 sections show significant dye extravasation for 0.64 MI compared to control with Evans blue and no microbubbles. Regions of significant dye extravasation outside of section 2 can also indicate blood-ventricular opening since those sections contain the choroid plexus. 18

Figure 7: (a) Schematic of the maximum intensity projection (MIP) generation process through taking the maximum of the 3D ultrasound localization microscopy along the sagittal direction. Representative example results are shown for 0.28 MI (b), 0.64 MI (c) and 0.78 MI (d), confirming that super-resolution images can be generated at ultrasound transmission settings used in this lab. MI: mechanical index 19

Figure 8: (a) Beam map of the ultrasound field measured through one of the 3 mouse skull caps in the plane directly in front of (and parallel to) the 3D transducer's surface. The hydrophone needle was centered under the skull cap and positioned 5mm under its point of highest curvature for measurements. The colormap represents acoustic peak negative pressure (in MPa), and the X and Y-axes represent the coordinates used to measure acoustic pressure delivered by the ultrasound transducer, sampled every 90 μm over a 110x110 grid. (b) Average max and minimum pressures varied greatly through the skull with a 70% variability between average max and min. 20

Figure 9: Fullwave 2 simulation results showing ultrasound transmission in a coronal slide through the 3 CT-scanned mouse skull caps in (a), (b) and (c). 21

LIST OF ABBREVIATIONS

BBB	Blood-brain-barrier
DFB	Decafluorobutane
EB	Evans blue
GPU	Graphics processing unit
MB	Microbubbles
MI	Mechanical index
OFP	Octofluoropentane
PBF	Phoasephate buffered formalin
PBS	Phosphate buffered saline
SR	Super resolution
US	Ultrasound

CHAPTER 1: INTRODUCTION & BACKGROUND

1.1 Medical Ultrasound

Ultrasound (US) is a physical acoustic wave that propagates at a frequency outside the range of human hearing (above 20 kHz). (1) This is done from a device known as a transducer, which contains piezoelectric material that produces the physical wave when a driving voltage is applied. US carries many benefits with it in the medical field. It is cheap, non-ionizing, well studied in its applications, and has numerous applications to treat and image the body for medical purposes. US has a wide range of applications such as fetal imaging, (2) doppler blood flow imaging, (3) and lithotripsy, (4) for example. There are limitations to US as well, the acoustic waves can be greatly impacted by the medium it is transmitted towards such as bone and tissue and the resolution of standard b-mode images is limited by the frequency of the transmitted wave. However, research has been done to overcome these limitations.

1.2 Super Resolution

Super Resolution (SR) imaging, also referred to as ultrasound localization microscopy (ULM), is an emerging US imaging technique which resolves the microvasculature beyond the diffraction limits of conventional US. One enabling requirement for SR imaging is the detection of spatiotemporally separable scatterers in the blood to delineate the microvasculature flow. (5) This is typically performed with microbubble (MB) contrast agents, though other scatterers can be used as well (phase-change contrast agents or red blood cells for example). (5–7) These acoustic scatterers are then infused, imaged, and then filtered to remove noise such as slow-

moving tissue. (8) MBs are localized in each frame, accumulated, and then tracked to delineate the microvasculature with sub-wavelength resolution. Further information, such as blood velocity and vessel diameter, can be extracted from this dataset by tracking the localized MBs over time. (5,8) One application where SR US has found broad application is in the brain, where the ability to visualize vascular structures and measure function has shown promise in assessment of diseases such as stroke, glioblastoma, and Alzheimer's disease. (9–15)

1.3 Blood-Brain-Barrier

MB contrast agents have been used clinically for decades and have demonstrated a safe application profile with standard diagnostic imaging conditions. (16) However, it is also known that within the brain, contrast–enhanced ultrasound (CEUS) is capable of causing bioeffects, such as modulation of the blood brain barrier (BBB). For example, studies have shown BBB opening with focused ultrasound can improve symptoms of Alzheimer disease in mice and allow for reversible BBB opening, (9,17) and BBB opening is currently studied in clinical trials to evaluate the potential of increasing chemotherapeutic delivery to the brain. (18)

The BBB is part of the vasculature in the central nervous system that protects the brain by reducing the permeability of both endogenous and exogeneous molecules. (18) This barrier includes the tight endothelial junctions, astrocytes, pericytes, and glycocalyx. (19,20) BBB opening is the phenomena where the permeability of the microvascular tissue barrier is increased, which can allow substances larger than 400 Da to pass through the tight endothelial junctions in the brain. (21) The BBB can be opened by traumatic brain injuries, diseases such as Alzheimer's, stroke, etc. (22,23)

1.4 Blood-Brain-Barrier Disruption

Research on BBB disruption, also known as BBB opening, by ultrasound has existed for decades, with one of the oldest studies being from the 1950s. (24) However, it's only until the past 2 decades, that strong interest in US assisted BBB disruption has gain traction for therapeutic applications. The introduction of microbubble contrast agents helped to achieve BBB disruption to treat brain diseases via drug delivery, (25,26) neuromodulate the brain, (27,28) and has been investigated for a wide variety of models, such as ovine, (29) non-human primates, (30–32) and murine, (33–35)and humans. (31,36–38)

There are numerous studies that have opened the BBB with focused ultrasound and MBs. Many studies use a focused transmit sequence due to numerous benefits such as the ability to reach higher pressures at lower driving voltages and a tighter region of sonication. For example, Choi et al had built a custom transducer that was intended to deliver drugs at a targeted region. (39) Another study had also used focused CEUS at sub megahertz frequencies to stimulate nerves of rat brains transcranially. (35)

It has also been demonstrated that the BBB can be reversibly opened with ultrasound in conjunction with MBs. There are numerous acoustic-mechanical effects involved in contrast-enhanced BBB disruption, including cavitation/MI, radiation force, and mechanical stresses. (40) Cavitation contributes to BBB disruption due to the oscillations of contrast agents, causing changes to the diameter of the MBs and pushing on the tight endothelial junctions. (40) The higher the pressure used can also impact the size of BBB opening. (41) This effect is further enhanced as the MBs are pushed towards the vascular endothelium by radiation force. (40) Typically, BBB modulation with focused ultrasound occurs when contrast agents are excited in the brain at low frequencies (0.2 to 1.05 MHz), at a peak negative pressure around 0.5 to 1.15

MPa, (40) and long duty cycles. Low frequencies have been preferred due to their reduced attenuation through the skull. For example, Kim et al. use a sub-MHz transmit for transcranial transmit. (35) The longer wavelength also helps to reduce effects of phase aberrations through the skull. Examples of this can be seen in O'Reilly et al. (42) and Hynynen et al. (43) More recent studies have also demonstrated BBB disruption with lower duty cycles. For example, studies have demonstrated BBB disruption in mice with a low duty cycle (0.5-1.25%) at 1-1.1 MHz. (44,45)

1.5 Thesis Outline

Most studies characterizing the threshold for BBB disruption as a function of certain ultrasound parameters, such as the mechanical index (MI) or bubble cavitation behavior through passive acoustic measurements, (46,47) have been performed in the context of focused ultrasound transmission for intentional BBB disruption. Multiple studies have demonstrated that BBB disruption is possible with clinical scanners using imaging sequences, including higher frequencies, shorter pulses and/or larger sonicated areas. Many studies have used commercial linear transducers, usually intended for imaging, to induce BBB opening with a focused sequences and contrast. For example, Bing et al. demonstrated BBB disruption with color Doppler at a 0.07% duty cycle with a 5.7 MHz transmit. (48) Zhao et al. showed that a phased array transducer with MBs caused BBB disruption at MIs from 0.2 to 0.8 at 1.5 MHz transmit. (49) Other studies have also shown BBB disruption using transmits identical to the 1.5 MHz transmit but with varying parameters such as MIs and transducers such as 1.3 MI and a Philips P4-1 (Philips Ultrasound, Bothell WA, USA) or 1.3 MI and a S5-1 transducer (Philips Ultrasound, Bothell WA, USA). (32,50) Yang et al. had also studied the effects of long-term

clinical imaging on the BBB of prenatal rats with a C5-2 (Philips Ultrasound, Bothell WA, USA) and found BBB disruption days after postnatal. (51)

This study aims to examine the potential for BBB disruption after 3D transcranial US SR imaging with MB contrast agents. Recent studies have demonstrated transcranial 3D SR imaging at 7.8 MHz. For example, Chavignon et al. tested SR images of the rat brain with a multiplexed matrix probe. (52) This study used a 67% duty cycle for 3D transcranial SR rat brain imaging. (52) Another example, by Demeulenaere et al. conducted transcranial SR imaging on a mouse with the same probe as Chavignon et al., with plane wave compounding, and a PRF between 182-750 kHz. (52,53) Transcranial SR US was also recently demonstrated in humans, including a healthy subject and patients from the stroke unit/neurovascular ward. (54)

US transmission through the skull can be affected by inhomogeneity and geometry. (55) For example, results from O'Reilly et al. showed that US wavelengths approaching the thickness of the skull generate distortions which had an effect on pressure distributions through the skull. (42) Thus, US transmission paths and pressure, at higher frequencies, can be impacted by the skull. It is recommended on the FDA label of Definity, (56) that the MI should not exceed 0.8 MI during contrast imaging. The American Institute of Ultrasound in Medicine recommends that contrast imaging with an MI above 0.4 should be minimized. (57) However, plane wave imaging at MIs below 0.4, calculated using a single derating value may result in areas of greater than expected pressure values due to not accounting for skull heterogeneity. To quantify the effects of 3D SR imaging on BBB opening, in this study, we use volumetric imaging with an 8 MHz Vermon (Vermon S.A., Tours, France) matrix array, transmitting a planewave compounding imaging sequence. We evaluate BBB opening, as observed from Evans Blue (EB) Dye extravasation on fluorescence imaging ex vivo, at non-derated transmitted MIs of 0.28, 0.64, and

0.78. However, the acoustical field inside the skull is highly heterogeneous and a scalar MI value does not capture this complex acoustical environment. We therefore also a) conduct pressure measurements through ex vivo skull caps and b) conduct ultrasound simulations in intact skulls with CT-derived models, to quantify the effects of ultrasound attenuation and lensing to relate heterogeneous intracranial acoustical distributions to our experimental results.

CHAPTER 2: METHODOLOGY

2.1 Animal Experiments

Studies were performed to quantify BBB disruption during contrast-enhanced, 3D super resolution brain imaging. All in-vivo experiments were performed with approval by the UNC Institutional Animal Care and Use Committee. 31 CD-1 mice (Female, 12wks old, 20-40 g) were used for 3 experimental groups (n= 8 per group) and one control group (n=7; one mouse from the control group reached a humane euthanasia endpoint early and could not serve as a control, preventing it from being used for analysis).

The main experimental steps are summarized in Fig. 1.

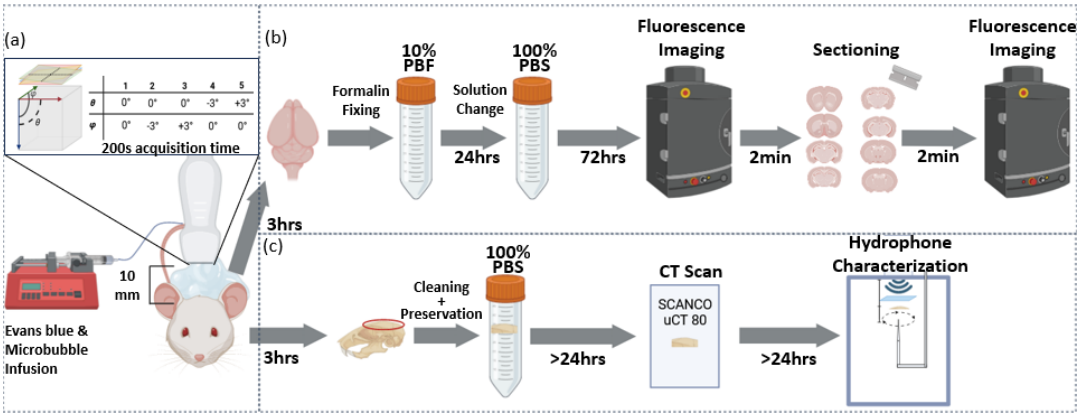

Figure 1: (a) Schematic of ultrasound (US) imaging and infusion setup. CD-1 mice were injected with 2 % Evans blue dye then followed by a bolus injection of decafluorobutane microbubbles (MB). The MBs were then placed onto the infusion pump (15uL/min) for the rest of the time the animal was placed for acquisition. Volumetric ultrasound images were acquired using plane wave compounding using single cycle pulses (5 angles, 2500 Hz pulse repetition frequency, 500 volumes per second). (b) Schematic of the in-vivo workflow where the mouse brains were fixed in PBF and then fluorescence images were taken, sectioned, then imaged again. (c) Hydrophone characterization timeline starting from in-vivo experiment to skull extraction and cleaning to CT scans taken and then hydrophone characterization. Specimen were stored in 100% phosphate buffered saline until time of scanning and time for characterization.

MB contrast agents used for this study were comprised of a phospholipid monolayer and decafluorobutane (DFB) gas core and were fabricated in-house. (58) This includes a 1.5 mL lipid solution and a gas headspace of DFB (1 μm mean diameter and $2x10^{10}$ mL^{-1} concentration), which were agitated in a 3mL vial in a VialMix (Lantheus Medical Imaging, North Billerica, MA, USA).

Animals were anesthetized with vaporized 2% isoflurane carried by medical air. Cranial fur was removed with veterinary clippers and depilatory cream. The head was fixed onto a stereotaxic frame (Stoelting Co., Wood Dale, Illinois, USA) and ultrasound gel was placed to couple the transducer to the head. A 2% solution of EB Dye (SIGMA-Aldrich, St. Louis, MO. 4 mL/kg) in phosphate buffered saline (1X PBS) was injected, as previously reported in Song et al., (59) through a 27-gauge tail vein catheter, immediately followed by a 50 μL saline (0.9% NaCl) flush before imaging. EB is a commonly used reporter for BBB opening and because of its large molecular weight and affinity to bind to albumin, prevents it from crossing the BBB unless said barrier is disrupted. (60) Therefore, significant detection of EB between a control group and experimental group under fluorescence imaging indicates BBB disruption. For all experimental groups receiving ultrasound, a 30 μL bolus of MBs, diluted with 0.9% NaCl saline to a concentration of 1.8E8 $mL^{-1}g^{-1}$, was injected following the saline flush. The MB solution was then set to infuse at 15 μL/min throughout the rest of the acquisition (15 μL/min with a 1 mL syringe). One min of infusion was allowed to pass before the start of the acquisition to ensure the MBs infusion reached a steady state. Then after this wait time, the imaging acquisition sequence was activated (total duration = 200 s; total volume of MB solution for each animal = 65 μL). The control group received EB dye without contrast or ultrasound imaging. After ultrasound imaging, EB was allowed to circulate in the vasculature for 3hrs to avoid possible perfusion

defects, since BBB disruption induced by ultrasound has been shown to modulate cerebral blood flow after disruption. (61) During this time, the animals were allowed to wake up, return to their cage, and remained there until initiating transcardial perfusions.

Animals were then euthanized via anesthesia overdose. Transcardial perfusions were performed via infusion through the left ventricle outflowing through an incision on the right atrium. First, 10 mL of PBS were perfused to clear out blood from the vasculature, followed by a perfusion of 10% formalin in a phosphate buffer solution (PBF) at a flow rate of 2mL/min to allow for brain tissue fixation.

Craniotomies were then performed to extract the brains. The brains were put into 10% PBF for further fixing over 24 hrs, and then washed with and placed into 100% phosphate buffered saline for 72hrs.

2.2 Ultrasound Imaging

For animals receiving ultrasound, transcranial SR imaging was performed using previously described sequences in McCall et al. (9,10) Briefly, planewave imaging at 7.81 MHz with 5 angles (3 degree) coherent compounding was transmitted via a Vermon 32x32 matrix array probe connected to a 4 system Vantage 256 (Verasonics, Kirkland, USA). The transducer was placed 10mm away from the mouse skull to avoid noise from the other angle transmits and reverberations. Planewave imaging was conducted immediately after injection of EB and MBs with a single cycle transmit and a PRF of 2500 Hz (500 volumes per second) for 200 s. The duty cycle was 0.03%.

Three different voltage settings were used, corresponding to an MI of 0.28, 0.64, and 0.78, as characterized using a hydrophone in water, in addition to the control, no ultrasound, case (MI = 0). The max MI, 0.78, was chosen as the highest pressure the Vermon probe could safely

transmit without risk of damage to the transducer. The middle MI of 0.64 was chosen as a pressure successfully used in our laboratory for 3D transcranial SR. Finally, the minimum MI, 0.28, was selected as half of the pressure corresponding to the middle MI, in order to have an intermediary pressure to test for potential bioeffects between no ultrasound and the pressure used for 3D SR in our laboratory.

2.3 Evaluation of BBB disruption

The brains were imaged under the IVIS spectrum (PerkinElmer Waltham, MA, USA) (excitation filter of 640 nm and an emission filter of 680 nm). Fluorescence images of the whole brain view were taken for every mouse brain in the study. In addition to whole brain fluorescence, we also quantified fluorescence intensity in individual coronal slices. This was to account for the possibility of blood-choroid barrier opening in the ventricles. In particular, section 2 corresponding to the region 2mm ahead of bregma was analyzed. 8 Coronal sections (1 mm thick) of the mouse brains were made after whole brain imaging with each section being 1mm thick, cutting the brain into 8 sections starting from the region of the brain 3 mm ahead of bregma, ending at 5 mm behind of bregma.

Whole brain fluorescence intensity was quantified as radiant efficiency in AURA 4.0.7 by drawing a rectangular region of interest (ROI) encompassing the whole brain while minimizing the area outside of the brain. Similarly, fluorescence intensity for each section was calculated by drawing ROIs encompassing each brain section. To evaluate which MI resulted in BBB disruption as indicated by significant dye extravasation, an ordinary 1-way analysis of variance (ANOVA) was performed on whole brain fluorescence intensity, as well as each section of the sectioned brain corresponding to different depths in the transverse direction. The mean

fluorescence intensity of the whole brain, or section, from each MI group was compared with the respective mean of the control group via Dunnet's multiple comparisons testing.

All statistical analyses were done in GraphPad PRISM (version 10.0.0 for Windows, GraphPad Software, Boston, Massachusetts USA, www.graphpad.com). Statistically significant differences were considered at $p < 0.05$. Data are presented as mean ± standard deviation, and statistical significance graphically depicted as *.

2.4 Super Resolution Processing

To validate that the parameters used for imaging were relevant for SR imaging, for each mouse, the acquired data was beamformed and processed off-line to create 3D SR images as described in McCall, et al. (9,10) Briefly, processing consisted of delay-and-sum beamforming on an isotropic grid with a step size of lambda/2 on a GPU workstation. Then, singular value decomposition (SVD) filtering was used to separate the fast-moving MB signal from the slower moving portions, including the skull and tissue. (5) This MB signal was localized using weighted centroids and was then tracked using the Hungarian algorithm (simpletacker). (62)

2.5 Ex-Vivo Characterization

To measure the skull's effect on ultrasound attenuation, aberration, and transmission patterns, acoustic characterization measurements were performed in a water tank using calvaria, as well as simulations of beam propagation through the skull and calvaria, were performed as follows.

For 3 animals from the control group, after euthanasia, the skull cap was removed through craniotomy and washed and placed in 100% PBS solution, then stored at 4C. The skulls were later scanned with a SCANCO μCT 80 with a 50-micron resolution capture (70 kVpp, 113 μA, 4 W) to allow for anatomical models to be imported and used for ultrasound simulations in

Fullwave 2 (described hereafter in **3D Simulations**). After scanning, the skulls were then epoxy-bonded to the side of the skull that would not be scanned under the transducer, degassed, and held in place while the hydrophone needle was moved with a 3-Axis motion stage for a 2D beammap.

Acoustic characterizations were performed in a water tank with an ONDA HNC-0200 hydrophone needle (ONDA Corporation, Sunnyvale, CA, USA). A single cycle, 0.64 MI transmit was delivered with the same probe used for the BBB experiments. Beam map of the ultrasound field measured through one of the 3 mouse skull caps in the plane directly in front of (and parallel to) the 3D transducer's surface. The hydrophone needle was centered under the skull cap and positioned 5mm under its point of highest curvature for measurements. Measurements occurred in a 110x110 (10mm x 10mm) size grid with 8 microseconds of data sampled 3 times and then averaged for each point. Maximum and minimum pressures through the mouse skull cap were averaged from multiple hotspots, for max and min separately, where a region of interest (ROI) mask is taken of the hotspot and then averaged within the ROI and then repeated for every hotspot.

In order to describe the local MI in the brain, descriptive statistics such as max, min, mean, and standard deviation of MI were calculated by taking an ROI over the map that was underneath the skull cap. The estimated descriptive statistics for the max transducer surface MI were also calculated. Statistics for the max transducer surface MI were calculated by generating an attenuation coefficient. These coefficients were made by taking the output hydrophone measurements (max, min, etc.) and dividing that by the transducer surface MI used for said measurements. The total area considered to have opened the BBB was calculated by rescaling the hydrophone measurements to the estimated descriptive statistics of the max transducer MI

and counting the total number of pixels that had an MI higher than the max MI the hydrophone had measured and then multiplying the count by the area of the hydrophone needle tip used for measurement (200 μm)

2.6 3D Simulations

Simulations were performed to characterize the full 3D acoustical field inside the murine skull from plane-wave transmits from the 8 MHz Vermon 32x32 matrix array. This allows a more accurate characterization of acoustical effects, including attenuation in the brain which cannot be ascertained from a hydrophone characterization. Simulations were performed using 3D Fullwave 2, an ultrasound simulation tool that uses a grid finite difference in the time domain (FDTD) approach to solve the wave equation with fourth order accuracy in time and up to 32nd order accuracy in space. (63–65) The acoustic maps of the skull caps were created using the CT scans as described in **Ex-Vivo Characterization.** The acoustic maps of the murine skull were created using the CT scan of a deceased mouse from Dogdas et al. (66) All 3 skull caps and the whole skull were used for simulations. All skull caps and the whole skull were segmented and converted from Hounsfield to acoustic parameters including sound speed, density, and attenuation. The speed of sound in the skull was generated assuming a maximum speed of sound of 2900 *m/s* and the density assuming a maximum of 2200 kg/m^3. (67) The attenuation map was generated using the following formula from Aubry et al. (68):

$a = amin + (amax - amin) * \phi 3$

where α is the attenuation and ϕ is the porosity estimated from the Hounsfield units, calculated from:

$$\phi = 1 - \frac{H}{1000}$$

where H represents the Hounsfield values. (68)

Parameters include a points per wavelength of 12, CFL = 0.2, 72hrs run time, and a 16.4319-micron grid size. The output includes an intensity plot in decibels with a color bar ranging from 0 to -45 dB. The total volume of the ultrasound beam through the skull that was considered to open the BBB was assumed where the MI was greater than the highest MI through the skull, seen in hydrophone measurements. The total volume was calculated by counting each voxel that had an MI higher than the hydrophone measurements max inside a volumetric cube, starting from the lowest point of the skull to 5mm below, 10 mm wide, and 10 mm in length. The total count was then multiplied by the voxel volume size. Percentage of the volume of BBB opening was calculated by taking the volume of the BBB opening capable region divided by the volumetric cube used.

CHAPTER 3: RESULTS & DISCUSSION

3.1 BBB Disruption Analysis

Fluorescence whole brain images and sectioned fluorescence images of the coronal view were generated by imaging EB that remained in the brain after fixation with the IVIS Spectrum (Fig 2 & Fig 3). As MI increases, the mean fluorescence intensity increases approximately $1x10^9$ $p^1s^{-1}cm^{-4}sr^{-1}\mu W^{-1}$.

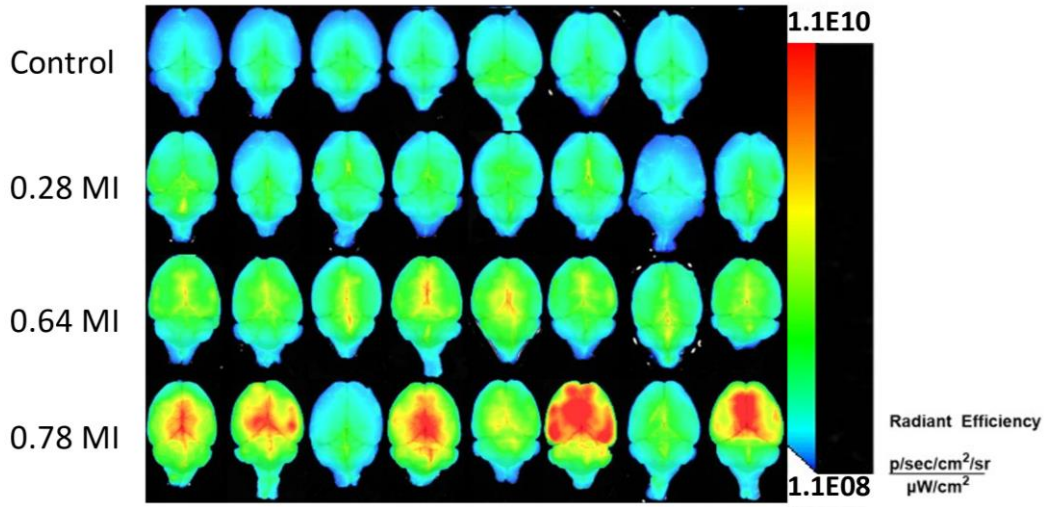

Figure 2: Whole brain fluorescence images showing the fluorescence intensity distribution per group. As mechanical index (MI) increases, so does the fluorescence intensity of the whole brain view of the mouse brain indicating increasing dye extravasation.

Coronal sections (Organized by column where the top left section is 1 and the bottom right section is 8) quantified the trend of increasing dye extravasation (Fig 3a). Generally, as MI increased, the fluorescence intensity did too. However, the increase of dye extravasation between MI varied between sections. This is expressed in Fig 3(b) as a heatmap where each square indicates the mean fluorescence intensity of the section in the MI group.

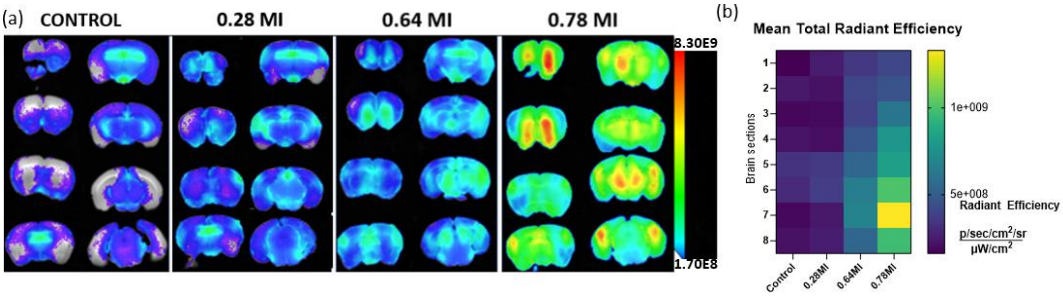

Figure 3: (a) Fluorescence images of all 8 coronal brain sections of one representative brain from each experimental group. (b) Heatmap of the fluorescence intensity from every section averaged from all 8 mouse brains per group. MI: mechanical index.

Example of what the sectioned slices looked like in AURA 4.0.7 from the first rounds of BBB study which also included an Evans blue with microbubble and no US group to test if there was a significant difference in dye extravasation between the control group used in the rest of the experiments. Significant dye extravasation was not seen between the groups thus the Evans blue and no microbubbles group was used as a control for the rest of the studies.

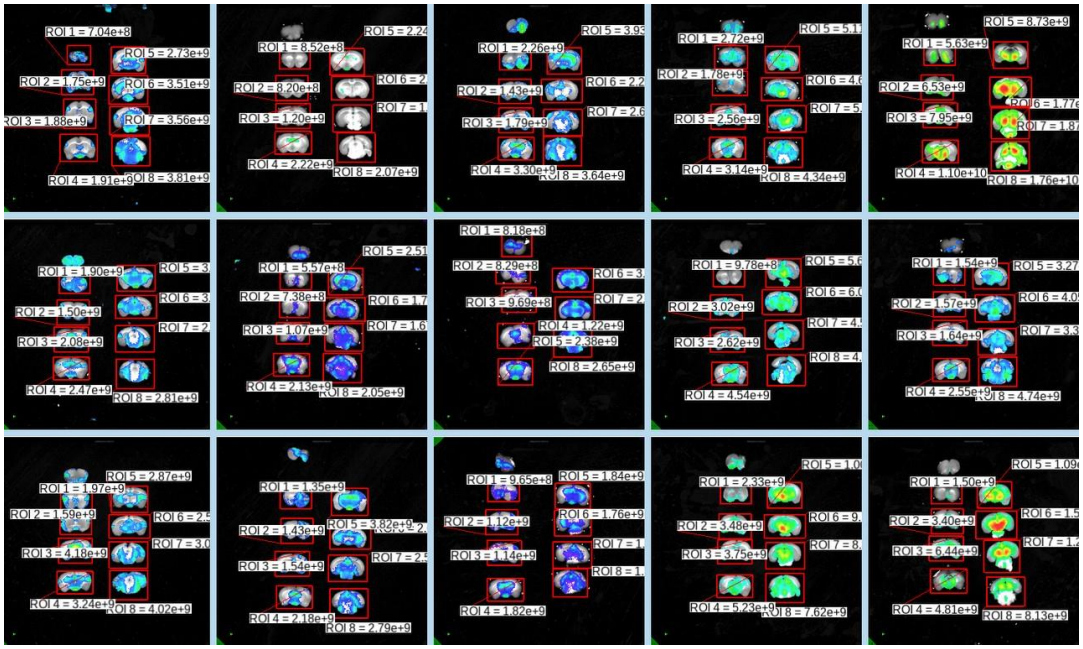

Figure 4: SECTIONED FLUORESCENCE IMAGES from the first rounds of the in-vivo study where each column represents 1 group (Evans blue dye and no microbubbles, Evans blue dye with microbubbles, 0.28 MI, 0.64 MI, and 0.78 MI). Dye extravasation increases with MI like in Fig 5a. The Evans blue dye with microbubbles group was found to have identical dye extravasation with the Evans blue dye with no microbubbles so the study was continued with the Evans blue dye with no microbubbles as the control group. The region of interest (ROI) rectangles can also be seen demonstrating how the ROI was drawn.

Dye extravasation was found to be significantly higher for 0.64 and 0.78 MI in whole brain fluorescence images compared to the no-ultrasound control (Fig.5a). However, only the fluorescence intensity of the 0.78 MI group was significantly increased when considering only coronal section 2 (Fig.5b).

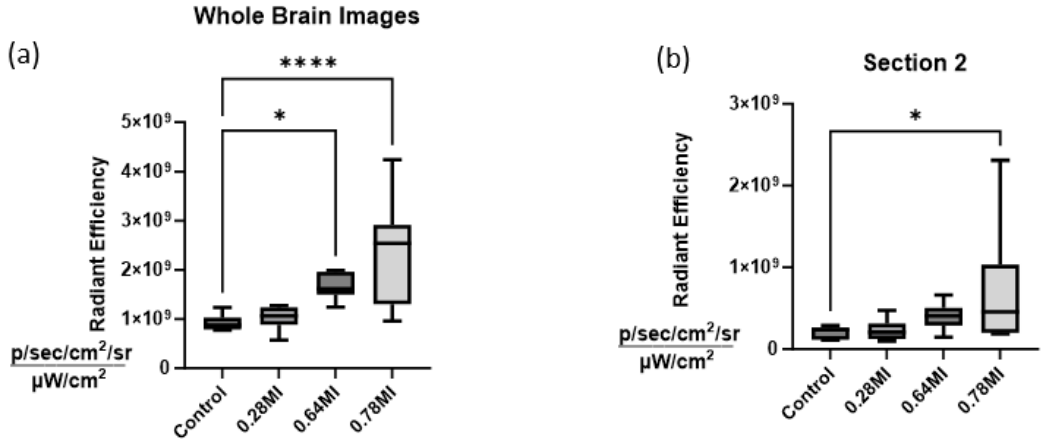

Figure 5: (a) Whole brain fluorescence intensity per experimental group. A significant increase in fluorescence intensity was observed for both 0.64 and 0.78 MI (MI = Mechanical Index) compared to the control group. (b) fluorescence intensity for a single brain section 2 mm in front of bregma, showing a significant increase in fluorescence intensity for 0.78 MI vs the control group.

Statistical tests were done on all other sections as well. Statistical significance was found for 0.64MI at section 6 and 7.

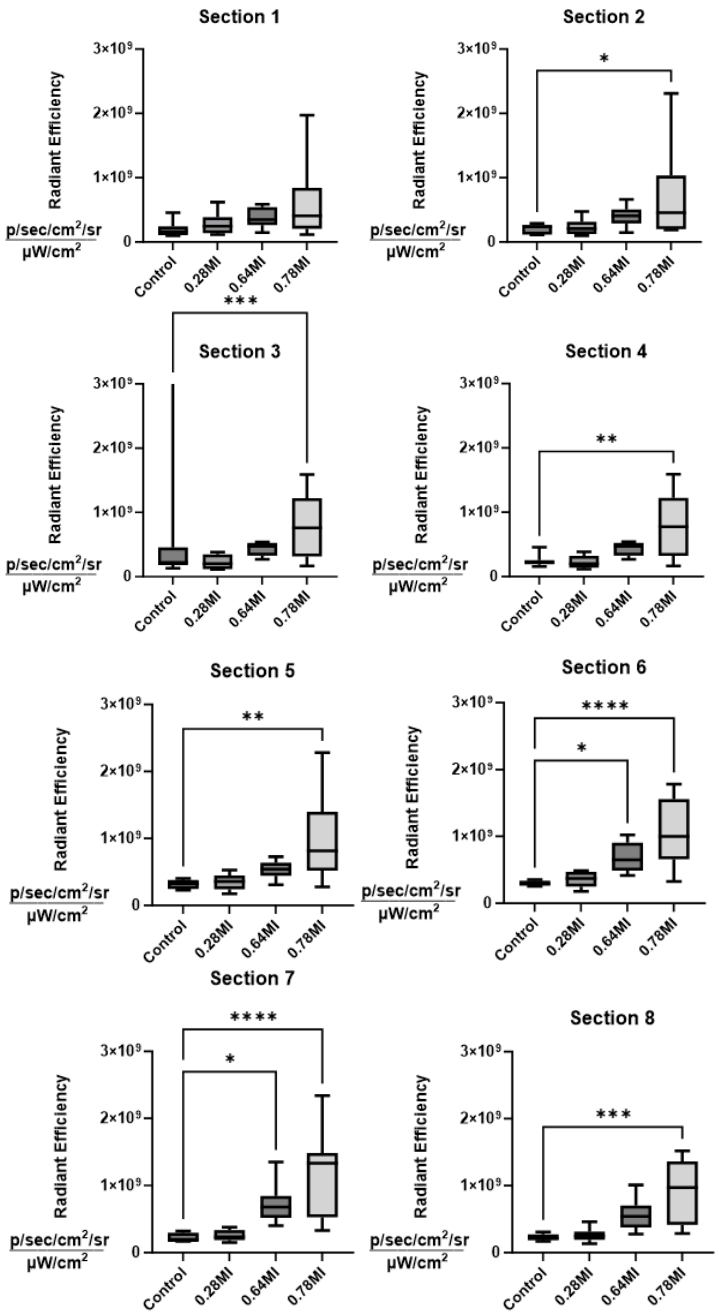

*Figure 6: Graphs of each section and results of Dunnet multiple comparisons test, shown as * for significant dye extravasation ($p<0.05$) from control. Every section except for section 1 showed significant dye extravasation for 0.78 MI and 2 sections show significant dye extravasation for 0.64 MI compared to control with Evans blue and no microbubbles. Regions of significant dye extravasation outside of section 2 can also indicate blood-ventricular opening since those sections contain the choroid plexus.*

3.2 Super Resolution

Data of the BBB experiments were processed in the ULM pipeline and rendered as maximum intensity projection from each MI group. (Fig 7) This demonstrated that super-resolution images are possible at the parameters used in this lab.

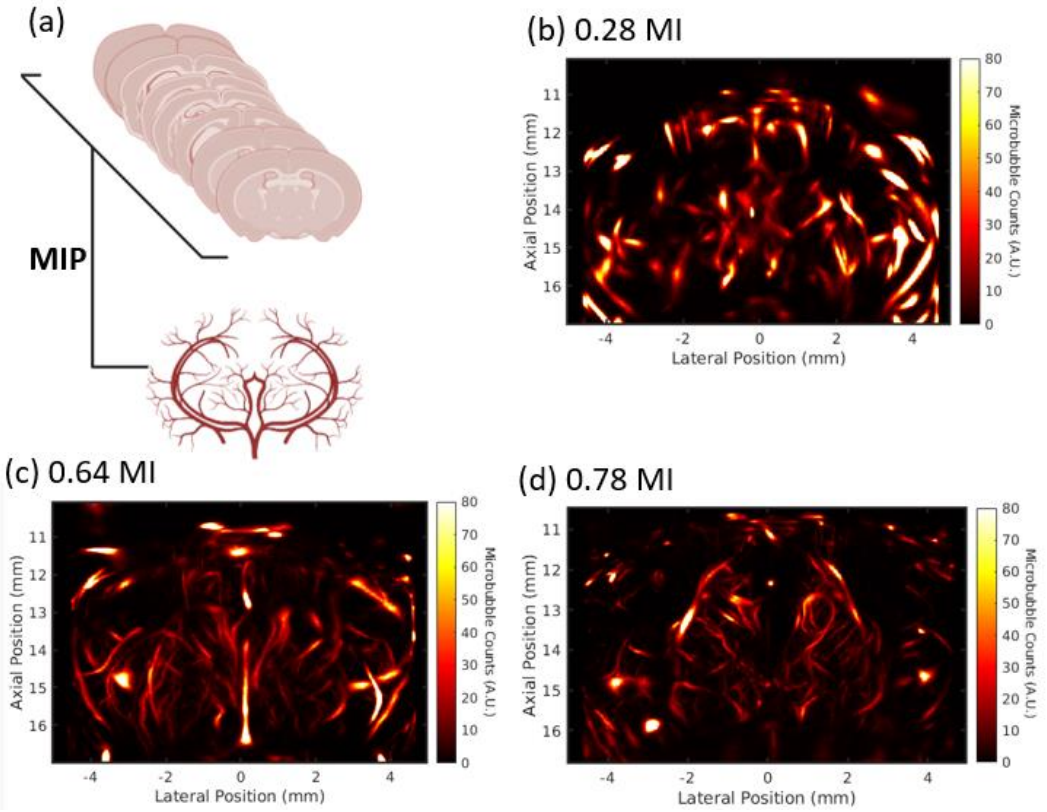

Figure 7: (a) Schematic of the maximum intensity projection (MIP) generation process through taking the maximum of the 3D ultrasound localization microscopy along the sagittal direction. Representative example results are shown for 0.28 MI (b), 0.64 MI (c) and 0.78 MI (d), confirming that super-resolution images can be generated at ultrasound transmission settings used in this lab. MI: mechanical index

3.3 Hydrophone Characterization

Hydrophone characterization showed a heterogeneous transmission of 3D planewave ultrasound through the murine skull (Fig 8). Peak negative pressure was seen to peak above 1 MPa with regions of hotspots.

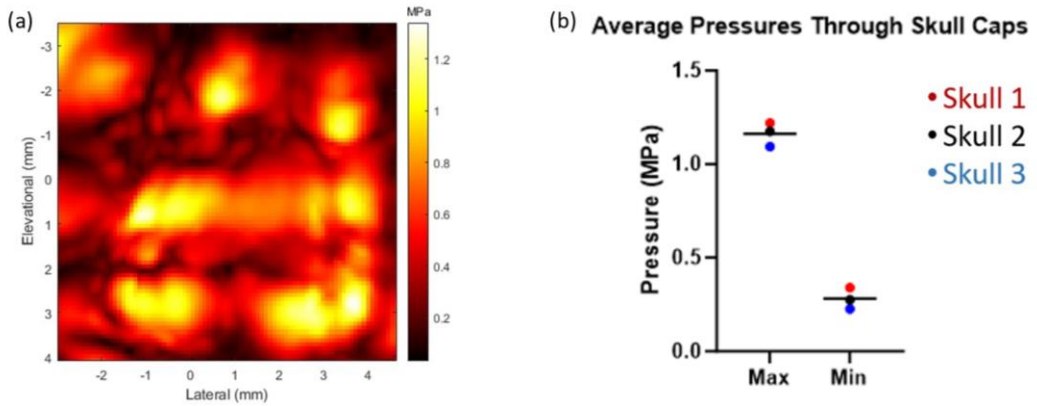

Figure 8: (a) Beam map of the ultrasound field measured through one of the 3 mouse skull caps in the plane directly in front of (and parallel to) the 3D transducer's surface. The hydrophone needle was centered under the skull cap and positioned 5mm under its point of highest curvature for measurements. The colormap represents acoustic peak negative pressure (in MPa), and the X and Y-axes represent the coordinates used to measure acoustic pressure delivered by the ultrasound transducer, sampled every 90 µm over a 110x110 grid. (b) Average max and minimum pressures varied greatly through the skull with a 70% variability between average max and min.

Average estimates of the local MI within the brain for a transducer surface MI of 0.64 were a max of 0.44 MI, min of 0.03 MI, average of 0.18 MI, and a standard deviation of 0.09 MI. For these values no significant BBB opening was observed. Estimates of the local MI for a transducer surface MI of 0.78 were a max of 0.53 MI, min of 0.04 MI, average of 0.22 MI, and a standard deviation of 0.11 MI. The total area of the brain that has a pressure above 0.44 was 4.828 mm^2 or 4.828% of the area scanned in our hydrophone measurements.

3.4 3D Simulations

3D simulation results showed effects of US transmission through the skull that the 200-micron resolution, hydrophone characterization could not show such as the high-resolution view of the US beam path through the skull. The ultrasound beam can be seen being redirected due to the curvature of the skull and generate focal hotspots (Fig 9). This effect was consistently seen in each of the simulations from the 3 skull caps.

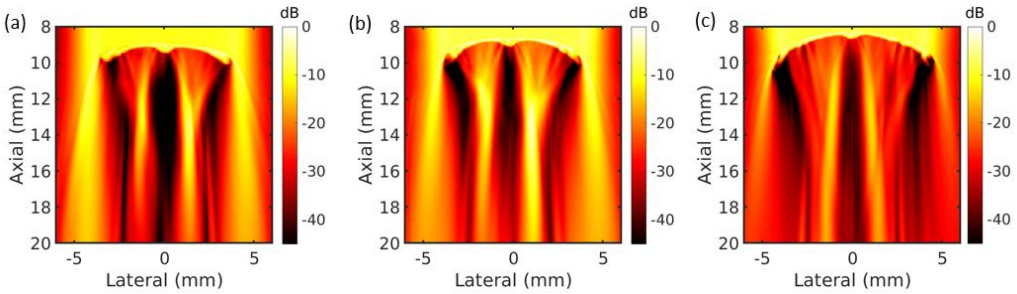

Figure 9: Fullwave 2 simulation results showing ultrasound transmission in a coronal slide through the 3 CT-scanned mouse skull caps in (a), (b) and (c).

The total volume of the brain that has a pressure above 0.44 was an average total volume 55.5 mm^3 or 11.10% of the volume underneath the skull.

3.5 BBB Disruption Discussion

The 3D SR US parameter tested in this study achieved BBB disruption with planewave imaging. This is the first time the Vermon 32x32 8 MHz matrix array has been seen to cause BBB disruption with CEUS at MIs below a recommended imaging limit in a commercial contrast agent. Prior studies using a diagnostic US system used sequences intending to open the BBB, usually with a focused sequence for targeting select regions and generating the high pressure needed. Studies such as Bing et al. and Zhao et al., reached BBB opening with a 0.2 MI (in-situ; through the skull using a single derated value) and 0.4 MI (transmitted) respectively, in mice. (48,49) In the case of this study, BBB disruption was not observed at 0.64 MI but was observed at 0.78 MI (transmitted MIs). The difference in MI needed for BBB disruption may be explained by the number of MBs delivered or the total number of cycles delivered. Song et al has previously shown using MB gas volume as a unifying dose parameter for BBB opening. (59) Thus, allowing for comparisons between studies that report different dosage variables such as mL/kg or total volume injected. So, using the number of microbubbles delivered, it can be estimated how much dosage of gas volume is involved with BBB opening. Bing et al. used concentrations from 400-2400 µL/kg (10-60 µL; concentration = 10^{10} mL^{-1}; (70) 1-6x10^9 MBs)

of Definity, (48) higher than the recommended 10 µL/kg dosage. Zhao et al. tested an amount of 0.5-3.0 x10^7 MBs delivered. This study used a delivery of 0.288-5.76x10^9 MBs (1.44x10^7 g^{-1}). (71) Various diagnostic ultrasound studies involving BBB disruption have used a ratio of mL/kg or a bolus volume injection that varied depending on the size of the animal or dosage. For example, ratios of volume injected include 0.05 µL/g, 0.02 mL/kg, and 1.5 mL/kg for OFP gas core MBs like Definity. (72–74) Other studies use a single volume for injection, usually 30 µL, which was 3X the recommended dosage at 3x10^8 MB injected. However, something to note is there is a limitation between comparing contrast dosage. Anesthetic carrier gas has a direct impact on bubble circulation and BBB disruption, (75) but the total dosage delivered still help to begin as a starting point in conversation about BBB opening via imaging transducers.

A comparison between bolus and infusion rate on BBB disruption has been compared before. For example, O'Reilly et al., compared infusion rates to bolus injections of Definity MBs, there they found that BBB disruption was found to be consistent for infusion but less effective than a bolus injection. (76) Thus, this study's results could explain the required increased MI needed to get significant amounts of dye extravasation compared to a control than other studies.

Some mice brains in the max pressure group however showed an interesting result where the fluorescence intensity was identical to the control group for both whole brain and sectioned views. This could be due to the angle of incidence varying slightly and reducing the focusing effect the skull had.

A confounding effect that needs to be accounted in evaluating BBB opening with Evans blue is the possibility of opening of the blood-choroid barrier in the ventricles. The ventricles are a part of the brain that also have their own barrier similar to the BBB but is known to be more

readily opened which can be seen in our own data and in Bing et al. (48) Specifically, we observe an increase in whole brain fluorescence intensity starting at 0.64MI (Fig.7a) but this is not the case when looking at section 2 only (Fig.7b) which shows only 0.78MI as resulting in significant fluorescent intensity increase. This is also visually apparent in Fig. 6a. Similarly to Bing at al., our interpretation of BBB opening therefore focuses on regions excluding the ventricles to remove the confounding effects of potential blood-ventricular opening. (48)

Section 7, which contains part of the choroid plexus, showed significant dye extravasation at 0.64 and 0.78 MI, similarly to the whole brain results. However, this result does not necessarily indicate BBB disruption for 0.64 MI as the blood-ventricular barrier is in said region and is known to be more readily opened than the BBB. (48)

Of note, fluorescence in section 2, being 2mm ahead of bregma, was of particular interest to observe the depth of possible BBB disruption in a region not including the choroid plexus, similarly to the analysis in Bing et al. (48) The choroid plexus contains a similar but different barrier called the blood-ventricular barrier, which is known to open more easily than the BBB. (48) So, testing on section 2 avoids noise from possible effects of blood-ventricular barrier opening.

3.6 Super Resolution Discussion

3D US SR images had an interesting effect based on MI. The amount of vasculature seen in the cortical region looked to have been maximized with the 0.64 MI case. This can be explained by the in-situ MI barely reaching above the point of inertial cavitation (0.4MI) and being high enough pressure for the transducer to capture the MB response through the skull. The 0.78 MI US parameter is capable of achieving and MI higher than 0.4 and over a larger region

than the 0.64 MI case which could cause MB destruction and eliminate the needed scatterer for localization and tracking.

An interesting phenomenon is that the middle experimental MI showed more vasculature than either group possibly due to higher echogenic response to MBs compared to 0.28 MI and low enough to avoid inertial cavitation with 0.78 MI.

3.7 Ultrasound Transmission Through the Murine Skull

Diagnostic US BBB disruption studies have also used regions of the brain that were not targeted and use those regions to compare dye extravasation of the treated areas. This method of comparison is not possible with 3D US transmit as the whole brain is treated. Thus, this study required a control group that received no US. 3D planewave US transmit of the matrix probe used for this study allows for testing whole brain BBB disruption since the aperture size of the transducer covers the whole mouse head. Another thing to consider is the 3D geometry of the skull in BBB disruption as the skull shape now plays a role in US transmission to the brain since the planewave transmit covers the whole head rather than a section of it. The hydrophone characterization reveals that the planewave transmit and high frequency are impacted by the geometry of the skull, which are effects noted by O'Reilly et al., for US wavelengths reaching the width of the skull. (42)

Attenuation and aberration result in a heterogeneous transmit through the mouse skull with a planewave transmit. Previous estimates for the loss of acoustic pressure through the skull were reviewed in Culjat et al., which found an attenuation and acoustic impedance of 6.9 $dB^{1}cm^{-1}MHz^{-1}$ respectively for cortical bone, 9.94 $dB^{1}cm^{-1}MHz^{-1}$ for trabecular bone, and 0.6 $dB^{1}cm^{-1}MHz^{-1}$ for the brain tissue itself. (77) Previously these values have been used to derate acoustic

pressure through rodent skulls to estimate focal pressure in the brain during noninvasive focused ultrasound (Gerstenmayer et al.). (78) They investigated acoustic transmission through multiple rat skulls and determined that reflection was a major contributor to insertion loss, compared to losses due to attenuation and aberration.

The differences in absolute acoustic pressure at any point in the skull may additionally be affected by the formation of reverberations, due to the frequency of ultrasound used for these applications and its relation to the size of the animal's skull cavity. Therefore, absolute pressure fields will vary from animal to animal and will change with the angle of incidence and position of the transducer, making a precise estimate difficult to translate for other studies.

In situ estimates of pressure allow us to relate the local acoustical environment within the brain and BBB to the transducer pressure values. Within the brain, at a transducer MI of 0.64, average estimates of the local MI within the brain were a max of 0.44 MI, min of 0.03 MI, average of 0.18 MI, and a standard deviation of 0.09 MI. For these values no significant BBB opening was observed. However, for a transducer MI of 0.78, local MI of max of 0.53 MI, min of 0.04 MI, average of 0.22 MI, and a standard deviation of 0.11 MI, BBB disruption was observed. This indicates that the local MI that generates BBB bioeffects is within a range of 0.44-0.53 MI. The total area of the brain that has a pressure above 0.44 was 4.828 mm^2 or 4.828% of the area scanned in our hydrophone measurements. However, one limitation regarding the measurements was that the needle hydrophone has a limited angular sensitivity due to the design of its needle. Simulations address the limited angular sensitivity due to its high spatial resolution capabilities to measure pressure precisely. The total volume that was considered to be above the lower pressure threshold of the MI range expected to open the BBB was 55.5 mm^3 or 11.10% under the skull in our simulations. One major limitation with simulation results however

is that the skull cap does not take into account the effects of reverberations and reflections from the bottom surface of an enclosed skull. Which if done would, more accurately represent estimates of acoustical pressure volume of BBB opening. Thus, whole skull simulations will be important to account for the whole skull changing the total volume of high MI regions.

Simulations also corroborate with the heterogeneous US transmission through the skull with a focusing effect noted with the skull cap and effects of standing waves from whole skull simulations, indicating lingering effects of US after the initial transmission through the murine skull and can cause mechanical effects of infused MBs. One limitation however is that the simulations were all done with a zero angle transmit. Thus, a future work would include simulations with differing angles of incidence.

CHAPTER 4: CONCLUSION

Prior studies have shown that linear clinical ultrasound systems are capable of inducing BBB disruption. However, those systems were used with sequences intended to cause BBB disruption. In this study, a SR imaging sequence on CD-1 mice using Evans blue to measure dye extravasation in the brain was tested. The in-vivo studies revealed significant dye extravasation with a transmitted MI of 0.78. 3D planewave, US transmit, from the transducer used in the in-vivo study, through the mouse skull was also tested. Here, the measurements showed a heterogeneous pressure map through the skull. This was also seen in simulations as well, where the US transmit was also found to be heterogeneous to the point where a singular derating value could not reveal every pressure the brain would experience.

This study has shown that BBB disruption can be observed with 3D planewave transmissions at pressures under regulatory limits. Demonstrating the possibility of BBB disruption with 3D transcranial CEUS. Our study examined the effect between increasing MI and dye extravasation past the BBB. Demonstrating that the mouse skull can transform volumetric plane wave transmit into a focused beam and create high MI areas and disrupt the BBB. In-situ estimates of pressure allow us to relate the local acoustical environment within the brain and BBB to the transducer pressure values. Estimates of the local MI, for a transducer surface MI of 0.64, within the brain were a max of 0.44 MI, min of 0.03 MI, average of 0.18 MI, and a standard deviation of 0.09 MI. For these values, no significant BBB opening was observed. However, for a transducer surface MI of 0.78 significant BBB opening was observed with a local

max MI of 0.53 MI, min MI of 0.04 MI, average of 0.22 MI, and a standard deviation of 0.11 MI. This indicates that the local MI that generates BBB bioeffects is within a range of 0.44-0.53 MI. The total volume of the brain that has a pressure above the lower end of this range is 4.83% in our hydrophone measurements (4.83 mm^2 of the 100 mm^2 2D plane scanned) and 11.10% in our simulations (55.5 mm^3 of 500 mm^3). Future work would include a broader set of US sequences such as varying PRF and frequency. Whole skull simulations would also be conducted to measure the effects of the whole skull on regions of high MI capable of inducing BBB opening. It could also include a custom delay transmit to correct for aberrations introduced by the skull. We conclude that 3D CEUS can be used safely without any evidence of BBB disruption or can open the BBB, depending on the MI.

REFERENCES

1. Ultrasound [Internet]. [cited 2023 Nov 9]. Available from: https://www.nibib.nih.gov/science-education/science-topics/ultrasound

2. Reddy UM, Filly RA, Copel JA. Prenatal Imaging: Ultrasonography and Magnetic Resonance Imaging. Obstetrics and gynecology [Internet]. 2008 [cited 2023 Nov 9];112(1):145. Available from: /pmc/articles/PMC2788813/

3. Oglat AA, Matjafri MZ, Suardi N, Oqlat MA, Abdelrahman MA, Oqlat AA. A Review of Medical Doppler Ultrasonography of Blood Flow in General and Especially in Common Carotid Artery. J Med Ultrasound [Internet]. 2018 Jan 1 [cited 2023 Nov 9];26(1):3. Available from: /pmc/articles/PMC6029191/

4. Ghorbani M, Oral O, Ekici S, Gozuacik D, Kosar A. Review on Lithotripsy and Cavitation in Urinary Stone Therapy. IEEE Rev Biomed Eng. 2016;9:264–83.

5. Errico C, Pierre J, Pezet S, Desailly Y, Lenkei Z, Couture O, et al. Ultrafast ultrasound localization microscopy for deep super-resolution vascular imaging. Nature 2015 527:7579 [Internet]. 2015 Nov 25 [cited 2022 Oct 25];527(7579):499–502. Available from: https://www.nature.com/articles/nature16066

5. Deruiter RM, Markley EN, Rojas JD, Pinton GF, Dayton PA. Using Low-Boiling Point Phase Change Contrast Agent Activation Signals for Super Resolution Ultrasound Localization Microscopy. IEEE International Ultrasonics Symposium, IUS. 2019 Oct 1;2019-October:1934–6.

7. Jensen JA, Schou M, Andersen SB, Søgaard SB, Sørensen CM, Nielsen MB, et al. Fast super resolution ultrasound imaging using the erythrocytes. https://doi.org/101117/122612245 [Internet]. 2022 Apr 4 [cited 2023 Oct 28];12038:79–84. Available from: https://www.spiedigitallibrary.org/conference-proceedings-of-spie/12038/120380E/Fast-super-resolution-ultrasound-imaging-using-the-erythrocytes/10.1117/12.2612245.full

8. Christensen-Jeffries K, Couture O, Dayton PA, Eldar YC, Hynynen K, Kiessling F, et al. Super-resolution Ultrasound Imaging. Ultrasound Med Biol [Internet]. 2020 Apr 1 [cited 2023 Oct 28];46(4):865–91. Available from: https://pubmed.ncbi.nlm.nih.gov/31973952/

9. McCall JR, Santibanez F, Belgharbi H, Pinton GF, Dayton PA. Non-invasive transcranial volumetric ultrasound localization microscopy of the rat brain with continuous, high volume-rate acquisition. Theranostics [Internet]. 2023 [cited 2023 Oct 6];13(4):1235–46. Available from: https://pubmed.ncbi.nlm.nih.gov/36923540/

10. McCall JR, DeRuiter R, Ross M, Santibanez F, Hingtgen SD, Pinton GF, et al. Longitudinal 3-D Visualization of Microvascular Disruption and Perfusion Changes in Mice During the Evolution of Glioblastoma Using Super-Resolution Ultrasound. IEEE Trans Ultrason Ferroelectr Freq Control [Internet]. 2023 [cited 2023 Oct 27];PP. Available from: https://pubmed.ncbi.nlm.nih.gov/37756182/

11. Yi H ming, Lowerison MR, Song P fei, Zhang W. A Review of Clinical Applications for Super-resolution Ultrasound Localization Microscopy. Curr Med Sci [Internet]. 2022 Feb 1 [cited 2023 Oct 28];42(1). Available from: https://pubmed.ncbi.nlm.nih.gov/35167000/

12. Renaudin N, Demené C, Dizeux A, Ialy-Radio N, Pezet S, Tanter M. Functional ultrasound localization microscopy reveals brain-wide neurovascular activity on a microscopic scale. Nature Methods 2022 19:8 [Internet]. 2022 Aug 4 [cited 2023 Oct 28];19(8):1004–12. Available from: https://www.nature.com/articles/s41592-022-01549-5

13. Morisset C, Dizeux A, Larrat B, Selingue E, Boutin H, Picaud S, et al. Retinal functional ultrasound imaging (rfUS) for assessing neurovascular alterations: a pilot study on a rat model of dementia. Sci Rep [Internet]. 2022 Dec 1 [cited 2023 Oct 28];12(1):19515. Available from: /pmc/articles/PMC9663720/

14. Chavignon A, Hingot V, Orset C, Vivien D, Couture O. 3D transcranial ultrasound localization microscopy for discrimination between ischemic and hemorrhagic stroke in early phase. Scientific Reports 2022 12:1 [Internet]. 2022 Aug 26 [cited 2023 Oct 28];12(1):1–11. Available from: https://www.nature.com/articles/s41598-022-18025-x

15. Deffieux T, Demené C, Tanter M. Functional Ultrasound Imaging: A New Imaging Modality for Neuroscience. Neuroscience. 2021 Oct 15;474:110–21.

16. Tsai HC, Tsai CH, Chen WS, Inserra C, Wei KC, Liu HL. Safety evaluation of frequent application of microbubble-enhanced focused ultrasound blood-brain-barrier opening. Sci Rep [Internet]. 2018 Dec 1 [cited 2023 Oct 28];8(1):17720. Available from: /pmc/articles/PMC6286368/

17. Hynynen K, McDannold N, Sheikov NA, Jolesz FA, Vykhodtseva N. Local and reversible blood-brain barrier disruption by noninvasive focused ultrasound at frequencies suitable for trans-skull sonications. Neuroimage [Internet]. 2005 Jan [cited 2023 Oct 6];24(1):12–20. Available from: https://pubmed.ncbi.nlm.nih.gov/15588592/

18. McMahon D, O'Reilly MA, Hynynen K. Therapeutic Agent Delivery Across the Blood-Brain Barrier Using Focused Ultrasound. Annu Rev Biomed Eng [Internet]. 2021 Jul 13 [cited 2023 Oct 6];23:89–113. Available from: https://pubmed.ncbi.nlm.nih.gov/33752471/

19. Daneman R, Prat A. The Blood–Brain Barrier. Cold Spring Harb Perspect Biol [Internet]. 2015 Jan 1 [cited 2023 Oct 6];7(1). Available from: /pmc/articles/PMC4292164/

20. Jin J, Fang F, Gao W, Chen H, Wen J, Wen X, et al. The Structure and Function of the Glycocalyx and Its Connection With Blood-Brain Barrier. Front Cell Neurosci. 2021 Oct 7;15:739699.

21. Kadry H, Noorani B, Cucullo L. A blood–brain barrier overview on structure, function, impairment, and biomarkers of integrity. Fluids and Barriers of the CNS 2020 17:1 [Internet]. 2020 Nov 18 [cited 2023 Oct 6];17(1):1–24. Available from: https://fluidsbarrierscns.biomedcentral.com/articles/10.1186/s12987-020-00230-3

22. Xiao M, Xiao ZJ, Yang B, Lan Z, Fang F. Blood-Brain Barrier: More Contributor to Disruption of Central Nervous System Homeostasis Than Victim in Neurological Disorders. Front Neurosci. 2020 Aug 6;14:540353.

23. Chodobski A, Zink BJ, Szmydynger-Chodobska J. Blood-brain barrier pathophysiology in traumatic brain injury. Transl Stroke Res [Internet]. 2011 [cited 2023 Oct 28];2(4):492. Available from: /pmc/articles/PMC3268209/

24. Bakay L, Hueter TF, Ballantine HT, Sosa D. Ultrasonically produced changes in the blood-brain barrier. AMA Arch Neurol Psychiatry [Internet]. 1956 [cited 2023 Nov 1];76(5):457–67. Available from: https://pubmed.ncbi.nlm.nih.gov/13371961/

25. Choi JJ, Pernot M, Small SA, Konofagou EE. Feasibility of transcranial, localized drug-delivery in the brain of Alzheimer's-model mice using Focused Ultrasound. Proc IEEE Ultrason Symp. 2005;2:988–91.

26. de Maar JS, Rousou C, van Elburg B, Vos HJ, Lajoinie GPR, Bos C, et al. Ultrasound-Mediated Drug Delivery With a Clinical Ultrasound System: In Vitro Evaluation. Front Pharmacol [Internet]. 2021 Oct 19 [cited 2023 Nov 5];12. Available from: https://pubmed.ncbi.nlm.nih.gov/34737709/

27. Chu PC, Liu HL, Lai HY, Lin CY, Tsai HC, Pei YC. Neuromodulation accompanying focused ultrasound-induced blood-brain barrier opening. Scientific Reports 2015 5:1 [Internet]. 2015 Oct 22 [cited 2023 Nov 5];5(1):1–12. Available from: https://www.nature.com/articles/srep15477

28. Kim H, Taghados SJ, Fischer K, Maeng LS, Park S, Yoo SS. Noninvasive transcranial stimulation of rat abducens nerve by focused ultrasound. Ultrasound Med Biol [Internet]. 2012 Sep [cited 2023 Nov 5];38(9):1568–75. Available from: https://pubmed.ncbi.nlm.nih.gov/22763009/

29. Yoon K, Lee W, Chen E, Lee JE, Croce P, Cammalleri A, et al. Localized blood-brain barrier opening in ovine model using image-guided transcranial focused ultrasound. Ultrasound Med Biol [Internet]. 2019 Sep 1 [cited 2023 Nov 5];45(9):2391. Available from: /pmc/articles/PMC6693666/

30. Marquet F, Tung YS, Teichert T, Ferrera VP, Konofagou EE. Noninvasive, Transient and Selective Blood-Brain Barrier Opening in Non-Human Primates In Vivo. PLoS One [Internet]. 2011 [cited 2023 Nov 5];6(7):e22598. Available from: https://journals.plos.org/plosone/article?id=10.1371/journal.pone.0022598

31. Horodyckid C, Canney M, Vignot A, Boisgard R, Drier A, Huberfeld G, et al. Safe long-term repeated disruption of the blood-brain barrier using an implantable ultrasound device: a multiparametric study in a primate model. J Neurosurg [Internet]. 2017 Apr 1 [cited 2023 Nov 5];126(4):1351–61. Available from: https://pubmed.ncbi.nlm.nih.gov/27285538/

32. Ji R, Burgess M, Konofagou E. Transcranial Blood-Brain Barrier Opening and Power Cavitation Imaging Using a Diagnostic Imaging Array. IEEE International Ultrasonics Symposium, IUS. 2019 Oct 1;2019-October:2–4.

33. O'Reilly MA, Huang Y, Hynynen K. The impact of standing wave effects on transcranial focused ultrasound disruption of the blood-brain barrier in a rat model. Phys Med Biol [Internet]. 2010 Sep 21 [cited 2023 Nov 6];55(18):5251–67. Available from: https://pubmed.ncbi.nlm.nih.gov/20720286/

34. Xu Y, Cui H, Zhu Q, Hua X, Xia H, Tan K, et al. Unilateral Opening of Rat Blood-Brain Barrier Assisted by Diagnostic Ultrasound Targeted Microbubbles Destruction. Biomed Res Int [Internet]. 2016 [cited 2023 Nov 5];2016. Available from: https://pubmed.ncbi.nlm.nih.gov/27579317/

35. Kim H, Taghados SJ, Fischer K, Maeng LS, Park S, Yoo SS. Noninvasive transcranial stimulation of rat abducens nerve by focused ultrasound. Ultrasound Med Biol [Internet]. 2012 Sep [cited 2023 Nov 5];38(9):1568–75. Available from: https://pubmed.ncbi.nlm.nih.gov/22763009/

36. Rezai AR, Ranjan M, Haut MW, Carpenter J, D'Haese PF, Mehta RI, et al. Focused ultrasound-mediated blood-brain barrier opening in Alzheimer's disease: long-term safety, imaging, and cognitive outcomes. J Neurosurg [Internet]. 2022 Jul 1 [cited 2023 Nov 5];139(1):275–83. Available from: https://pubmed.ncbi.nlm.nih.gov/36334289/

37. McDannold N, Arvanitis CD, Vykhodtseva N, Livingstone MS. Temporary disruption of the blood-brain barrier by use of ultrasound and microbubbles: safety and efficacy evaluation in rhesus macaques. Cancer Res [Internet]. 2012 Jul 15 [cited 2023 Nov 5];72(14):3652–63. Available from: https://pubmed.ncbi.nlm.nih.gov/22552291/

38. Kobus T, Vykhodtseva N, Pilatou M, Zhang Y, McDannold N. Safety Validation of Repeated Blood-Brain Barrier Disruption Using Focused Ultrasound. Ultrasound Med Biol [Internet]. 2016 Feb 1 [cited 2023 Nov 5];42(2):481–92. Available from: https://pubmed.ncbi.nlm.nih.gov/26617243/

39. Choi JJ, Selert K, Vlachos F, Wong A, Konofagou EE. Noninvasive and localized neuronal delivery using short ultrasonic pulses and microbubbles. Proc Natl Acad Sci U S A [Internet]. 2011 Oct 4 [cited 2023 Nov 5];108(40):16539–44. Available from: /pmc/articles/PMC3189054/

40. Gandhi K, Barzegar-Fallah A, Banstola A, Rizwan SB, Reynolds JNJ. Ultrasound-Mediated Blood-Brain Barrier Disruption for Drug Delivery: A Systematic Review of Protocols, Efficacy, and Safety Outcomes from Preclinical and Clinical Studies. Pharmaceutics [Internet]. 2022 Apr 1 [cited 2023 Oct 6];14(4). Available from: https://pubmed.ncbi.nlm.nih.gov/35456667/

41. Chen H, Konofagou EE. The size of blood-brain barrier opening induced by focused ultrasound is dictated by the acoustic pressure. J Cereb Blood Flow Metab [Internet]. 2014 [cited 2023 Nov 5];34(7):1197–204. Available from: https://pubmed.ncbi.nlm.nih.gov/24780905/

42. O'Reilly MA, Muller A, Hynynen K. Ultrasound insertion loss of rat parietal bone appears to be proportional to animal mass at sub-megahertz frequencies. Ultrasound Med Biol [Internet]. 2011 Nov [cited 2023 Oct 6];37(11):1930. Available from: /pmc/articles/PMC3228246/

43. Hynynen K, McDannold N, Sheikov NA, Jolesz FA, Vykhodtseva N. Local and reversible blood–brain barrier disruption by noninvasive focused ultrasound at frequencies suitable for trans-skull sonications. Neuroimage. 2005 Jan 1;24(1):12–20.

44. Morse S V., Pouliopoulos AN, Chan TG, Copping MJ, Lin J, Long NJ, et al. Rapid short-pulse ultrasound delivers drugs uniformly across the murine blood-brain barrier with negligible disruption. Radiology [Internet]. 2019 May 1 [cited 2023 Oct 12];291(2):459–66. Available from: https://doi.org/10.1148/radiol.2019181625

45. Choi HJ, Han M, Seo H, Park CY, Lee EH, Park J. The new insight into the inflammatory response following focused ultrasound-mediated blood–brain barrier disruption. Fluids Barriers CNS [Internet]. 2022 Dec 1 [cited 2023 Oct 13];19(1):1–21. Available from: https://link.springer.com/articles/10.1186/s12987-022-00402-3

46. McDannold N, Vykhodtseva N, Hynynen K. Blood-brain barrier disruption induced by focused ultrasound and circulating preformed microbubbles appears to be characterized by the mechanical index. Ultrasound Med Biol [Internet]. 2008 May [cited 2023 Oct 6];34(5):834. Available from: /pmc/articles/PMC2442477/

47. Arvanitis CD, Livingstone MS, Vykhodtseva N, McDannold N. Controlled Ultrasound-Induced Blood-Brain Barrier Disruption Using Passive Acoustic Emissions Monitoring. PLoS One [Internet]. 2012 Sep 24 [cited 2023 Oct 6];7(9):e45783. Available from: https://journals.plos.org/plosone/article?id=10.1371/journal.pone.0045783

48. Bing KF, Howles GP, Qi Y, Palmeri ML, Nightingale KR. Blood-Brain Barrier (BBB) Disruption Using a Diagnostic Ultrasound Scanner and Definity® in Mice. Ultrasound Med Biol. 2009 Aug 1;35(8):1298–308.

49. Zhao B, Chen Y, Liu J, Zhang L, Wang J, Yang Y, et al. Blood-brain barrier disruption induced by diagnostic ultrasound combined with microbubbles in mice [Internet]. Vol. 9, Oncotarget. 2018. Available from: www.impactjournals.com/oncotarget

50. Zhang J, Liu H, Du X, Guo Y, Chen X, Wang S, et al. Increasing of Blood-Brain Tumor Barrier Permeability through Transcellular and Paracellular Pathways by Microbubble-Enhanced Diagnostic Ultrasound in a C6 Glioma Model. Front Neurosci [Internet]. 2017 Feb 23 [cited 2023 Nov 5];11(FEB). Available from: https://pubmed.ncbi.nlm.nih.gov/28280455/

51. Yang FY, Lin GL, Horng SC, Chen RC. Prenatal exposure to diagnostic ultrasound impacts blood-brain barrier permeability in rats. Ultrasound Med Biol [Internet]. 2012 Jun [cited 2023 Nov 6];38(6):1051–7. Available from: https://pubmed.ncbi.nlm.nih.gov/22424599/

52. Chavignon A, Heiles B, Hingot V, Orset C, Vivien D, Couture O. 3D Transcranial Ultrasound Localization Microscopy in the Rat Brain with a Multiplexed Matrix Probe. IEEE Trans Biomed Eng. 2022 Jul 1;69(7):2132–42.

53. Demeulenaere O, Bertolo A, Pezet S, Ialy-Radio N, Osmanski B, Papadacci C, et al. In vivo whole brain microvascular imaging in mice using transcranial 3D Ultrasound Localization Microscopy. EBioMedicine [Internet]. 2022 May 1 [cited 2023 Oct 6];79. Available from: https://pubmed.ncbi.nlm.nih.gov/35460988/

54. Demené C, Robin J, Dizeux A, Heiles B, Pernot M, Tanter M, et al. Transcranial ultrafast ultrasound localization microscopy of brain vasculature in patients. Nature Biomedical Engineering 2021 5:3 [Internet]. 2021 Mar 15 [cited 2023 Oct 28];5(3):219–28. Available from: https://www.nature.com/articles/s41551-021-00697-x

55. Clement GT, Hynynen K. Correlation of ultrasound phase with physical skull properties. Ultrasound Med Biol. 2002 May 1;28(5):617–24.

56. Lantheus Medical Imaging. Definity [Internet]. 2001 [cited 2023 Oct 28]. Available from: www.fda.gov/medwatch.

57. Statement on Biological Effects in Tissues with Ultrasound Contrast Agents [Internet]. [cited 2023 Oct 14]. Available from: https://www.aium.org/resources/official-statements/view/statement-on-biological-effects-in-tissues-with-ultrasound-contrast-agents

58. Rojas JD, Dayton PA. Vaporization Detection Imaging: A Technique for Imaging Low-Boiling-Point Phase-Change Contrast Agents with a High Depth of Penetration and Contrast-to-Tissue Ratio. Ultrasound Med Biol [Internet]. 2019 Jan 1 [cited 2023 Oct 7];45(1):192–207. Available from: https://pubmed.ncbi.nlm.nih.gov/30482709/

59. Song KH, Fan AC, Hinkle JJ, Newman J, Borden MA, Harvey BK. Microbubble gas volume: A unifying dose parameter in blood-brain barrier opening by focused ultrasound. Theranostics [Internet]. 2017 [cited 2023 Oct 7];7(1):144–52. Available from: https://pubmed.ncbi.nlm.nih.gov/28042323/

60. Goldim MP de S, Della Giustina A, Petronilho F. Using Evans Blue Dye to Determine Blood-Brain Barrier Integrity in Rodents. Curr Protoc Immunol [Internet]. 2019 Sep 1 [cited 2023 Oct 28];126(1). Available from: https://pubmed.ncbi.nlm.nih.gov/31483106/

61. Todd N, Angolano C, Ferran C, Devor A, Borsook D, McDannold N. Secondary effects on brain physiology caused by focused ultrasound-mediated disruption of the blood-brain barrier. J Control Release [Internet]. 2020 Aug 8 [cited 2023 Oct 7];324:450. Available from: /pmc/articles/PMC7429281/

62. GitHub - tinevez/simpletracker: A simple particle tracking algorithm for MATLAB that can deal with gaps. [Internet]. [cited 2023 Oct 7]. Available from: https://github.com/tinevez/simpletracker

63. Pinton GF, Dahl J, Rosenzweig S, Trahey GE. A heterogeneous nonlinear attenuating full-wave model of ultrasound. IEEE Trans Ultrason Ferroelectr Freq Control [Internet]. 2009 Mar [cited 2023 Oct 7];56(3):474–88. Available from: https://pubmed.ncbi.nlm.nih.gov/19411208/

64. Pinton G. A fullwave model of the nonlinear wave equation with multiple relaxations and relaxing perfectly matched layers for high-order numerical finite-difference solutions. 2021 Jun 22 [cited 2023 Oct 7]; Available from: https://arxiv.org/abs/2106.11476v1

65. Aubry JF, Bates O, Boehm C, Pauly KB, Christensen D, Cueto C, et al. Benchmark problems for transcranial ultrasound simulation: Intercomparison of compressional wave models. J Acoust Soc Am [Internet]. 2022 Feb 9 [cited 2023 Oct 7];152(2):1003–19. Available from: http://arxiv.org/abs/2202.04552

66. Dogdas B, Stout D, Chatziioannou AF, Leahy RM. Digimouse: a 3D whole body mouse atlas from CT and cryosection data. Phys Med Biol [Internet]. 2007 Feb 7 [cited 2023 Oct 7];52(3):577–87. Available from: https://pubmed.ncbi.nlm.nih.gov/17228106/

67. Duck FA. Acoustic Properties of Tissue at Ultrasonic Frequencies. Physical Properties of Tissues. 1990 Jan 1;73–135.

68. Aubry JF, Tanter M, Pernot M, Thomas JL, Fink M. Experimental demonstration of noninvasive transskull adaptive focusing based on prior computed tomography scans. J Acoust Soc Am [Internet]. 2003 Jan 1 [cited 2023 Oct 7];113(1):84–93. Available from: https://pubmed.ncbi.nlm.nih.gov/12558249/

69. Jones RM, Caskey CF, Dayton PA, Oralkan O, Pinton GF. Transcranial Neuromodulation Array With Imaging Aperture for Simultaneous Multifocus Stimulation in Nonhuman Primates. IEEE Trans Ultrason Ferroelectr Freq Control [Internet]. 2022 Jan 1 [cited 2023 Oct 7];69(1):261–72. Available from: https://pubmed.ncbi.nlm.nih.gov/34460372/

70. Tu J, Swalwell JE, Giraud D, Cui W, Chen W, Matula TJ. Microbubble Sizing and Shell Characterization Using Flow Cytometry. IEEE Trans Ultrason Ferroelectr Freq Control [Internet]. 2011 May [cited 2023 Oct 17];58(5):955. Available from: /pmc/articles/PMC4495763/

71. Zhao B, Chen Y, Liu J, Zhang L, Wang J, Yang Y, et al. Blood-brain barrier disruption induced by diagnostic ultrasound combined with microbubbles in mice. Oncotarget [Internet]. 2018 Jan 1 [cited 2023 Oct 6];9(4):4897. Available from: /pmc/articles/PMC5797021/

72. Choi JJ, Selert K, Vlachos F, Wong A, Konofagou EE. Noninvasive and localized neuronal delivery using short ultrasonic pulses and microbubbles. Proc Natl Acad Sci U S A [Internet]. 2011 Oct 4 [cited 2023 Oct 17];108(40):16539–44. Available from: /pmc/articles/PMC3189054/

73. O'Reilly MA, Huang Y, Hynynen K. The impact of standing wave effects on transcranial focused ultrasound disruption of the blood-brain barrier in a rat model. Phys Med Biol [Internet]. 2010 Sep 21 [cited 2023 Oct 17];55(18):5251–67. Available from: https://pubmed.ncbi.nlm.nih.gov/20720286/

74. Zhang J, Liu H, Du X, Guo Y, Chen X, Wang S, et al. Increasing of Blood-Brain Tumor Barrier Permeability through Transcellular and Paracellular Pathways by Microbubble-Enhanced Diagnostic Ultrasound in a C6 Glioma Model. Front Neurosci [Internet]. 2017 Feb 23 [cited 2023 Oct 17];11(FEB). Available from: https://pubmed.ncbi.nlm.nih.gov/28280455/

75. McDannold N, Zhang Y, Vykhodtseva N. The effects of oxygen on ultrasound-induced blood-brain barrier disruption in mice. Ultrasound Med Biol [Internet]. 2017 Feb 1 [cited 2023 Nov 16];43(2):469. Available from: /pmc/articles/PMC5191922/

76. O'Reilly MA, Waspe AC, Ganguly M, Hynynen K. Focused-Ultrasound Disruption of the Blood-Brain Barrier Using Closely-Timed Short Pulses: Influence of Sonication Parameters and Injection Rate. Ultrasound Med Biol [Internet]. 2011 Apr [cited 2023 Oct 17];37(4):587. Available from: /pmc/articles/PMC3062725/

77. Culjat MO, Goldenberg D, Tewari P, Singh RS. A review of tissue substitutes for ultrasound imaging. Ultrasound Med Biol [Internet]. 2010 [cited 2023 Oct 7];36(6):861–73. Available from: https://pubmed.ncbi.nlm.nih.gov/20510184/

78. Gerstenmayer M, Fellah B, Magnin R, Selingue E, Larrat B. Acoustic Transmission Factor through the Rat Skull as a Function of Body Mass, Frequency and Position. Ultrasound Med Biol. 2018 Nov 1;44(11):2336–44.